Review of Scientific Instruments

Multimodal real-time frequency tracking of cantilever arrays in liquid environment for biodetection: Comprehensive setup and performance analysis

Cite as: Rev. Sci. Instrum. **92**, 065001 (2021); https://doi.org/10.1063/5.0047631
Submitted: 15 February 2021 . Accepted: 14 May 2021 . Published Online: 02 June 2021

Annalisa De Pastina, Francesco Padovani, Giulio Brunetti, Chiara Rotella, Fabio Niosi, Victor Usov, and Martin Hegner

Review of Scientific Instruments ARTICLE scitation.org/journal/rsi

Multimodal real-time frequency tracking of cantilever arrays in liquid environment for biodetection: Comprehensive setup and performance analysis

Cite as: Rev. Sci. Instrum. 92, 065001 (2021); doi: 10.1063/5.0047631
Submitted: 15 February 2021 • Accepted: 14 May 2021 •
Published Online: 2 June 2021

Annalisa De Pastina,[1] Francesco Padovani,[2] Giulio Brunetti,[1] Chiara Rotella,[1] Fabio Niosi,[1] Victor Usov,[3] and Martin Hegner[1,a)]

AFFILIATIONS

[1] School of Physics, Center for Research on Adaptive Nanostructures and Nanodevices (CRANN), Trinity College Dublin (TCD), D02 Dublin, Ireland
[2] Institute of Functional Epigenetics, Helmholtz Zentrum München (HMGU), Neuherberg 85764, Germany
[3] School of Physics, Trinity College Dublin (TCD), D02 Dublin, Ireland

[a)] **Author to whom correspondence should be addressed:** hegnerm@tcd.ie

ABSTRACT

We present a nanomechanical platform for real-time quantitative label-free detection of target biomolecules in a liquid environment with mass sensitivity down to few pg. Newly fabricated arrays of up to 18 cantilevers are integrated in a micromachined fluidi chamber, connected to software-controlled fluidi pumps for automated sample injections. We discuss two functionalization approaches to independently sensitize the interface of different cantilevers. A custom piezo-stack actuator and optical readout system enable the measurement of resonance frequencies up to 2 MHz. We implement a new measurement strategy based on a phase-locked loop (PLL), built via in-house developed software. The PLL allows us to track, within the same experiment, the evolution of resonance frequency over time of up to four modes for all the cantilevers in the array. With respect to the previous measurement technique, based on standard frequency sweep, the PLL enhances the estimated detection limit of the device by a factor of 7 (down to 2 pg in 5 min integration time) and the time resolution by more than threefold (below 15 s), being on par with commercial gold-standard techniques. The detection limit and noise of the new setup are investigated via Allan deviation and standard deviation analysis, considering different resonance modes and interface chemistries. As a proof-of-concept, we show the immobilization and label-free *in situ* detection of live bacterial cells (*E. coli*), demonstrating qualitative and quantitative agreement in the mechanical response of three different resonance modes.

I. INTRODUCTION

In the past 20 years, microcantilever biosensors operated in liquid demonstrated outstanding sensing capabilities.[1–4] Several label-free nanomechanical assays have been developed, targeting the real-time detection of specifi biomarkers in physiological environment.[5,6] The detection of molecules of clinical interest such as proteins,[7] RNA,[8–10] and cells[11–15] achieved comparable or better performances to commercial gold-standard techniques. The most widely used method in clinical environment is the enzyme-linked immunosorbent assay (ELISA), which exhibits sub-picomolar limit-of-detection, but requires long analysis times, expensive reagents, and does not provide quantitative information.[16] We recently demonstrated a direct one-step label-free quantitative immunoassay investigating malaria vaccines, with cantilever arrays with a sensitivity that is on par with the gold-standard multi-step ELISA procedure in serum.[7] Other micro/nanomechanical technologies able to achieve the detection of biomolecules in liquid environment include quartz-crystal microbalance (QCM),[17] surface–plasmon resonance (SPR),[18] suspended microchannel resonators (SMR),[19]

surface acoustic wave (SAW) devices,[20] and membrane-type surface stress (MSS) sensors,[21] among others. An exhaustive overview and comparison of the above-mentioned technologies, as well as other biosensing techniques, is provided in the excellent review by Arlett *et al.*[22]

Operating the sensors in liquid is paramount in order to mimic physiological conditions and target clinical applications. However, in-flui operation adds a considerable level of complexity to the experimental procedure, requiring thorough engineering of the experimental protocol and measurement setup.[23] The transduction strategy needs to be selected and implemented while taking into account the mechanical damping caused by the liquid around the resonators, so as to maximize the signal-to-noise ratio, thus boosting sensing performance.

Analytes binding to the sensitized surface of a cantilever sensor can be detected evaluating either the stress-induced quasi-static deflectio (static mode operation) or via the mass-induced resonance frequency shift (dynamic mode operation). Cantilever mechanical behavior is strongly affected by the surrounding medium and environmental changes (e.g., temperature, viscosity, and pH),[24–26] which constitute competitive effects toward the biomolecular recognition. The best strategy to circumvent these effects is to use multiple microcantilevers on the same chip. Microfabricated cantilever arrays present a number of advantages: (i) internal control toward unspecifi binding can be achieved by passivating the interfaces of selected sensors; (ii) possibility to perform a differential readout among multiple sensors. This allows us to correct for thermal drifts or environmental changes, but it also makes possible to compare the binding of the same analyte to different surfaces or antigens;[7] (iii) the mechanical response from sensors sensitized with the same biochemical functionalization can be averaged, thus increasing statistical robustness of experimental results; (iv) possibility to study multiple biochemical interactions within the same experiment; (v) reduction in time and cost of a single test.

In this paper, we provide the comprehensive description of a nanomechanical platform for real-time quantitative label-free detection of target biomolecules in liquid environment with mass sensitivity down to few pg. We include a short description of the device microfabrication process and functionalization strategies. With respect to our previous publications, we introduce a larger cantilever array with up to 18 sensors that allow more versatility in functionalization and averaging of identically sensitized sensors. Moreover, we describe a newly implemented measurement strategy for dynamic mode analysis, via a phase-locked loop (PLL). This approach allows us to track the evolution of the resonance frequency over time of up to 4 resonance modes, for as many sensors as needed (18 in this work). The introduction of the PLL tracking enhances the estimated detection limit of the device by a factor of 7. A custom-built piezoceramic stack actuator, together with an optimized optical readout system, provides access to a measurement frequency range between 1 kHz and 2 MHz. Furthermore, we perform an analysis of the frequency noise and an estimation of sensing capabilities of our measurement setup, considering different resonance modes and interface chemistries. As a proof-of-concept, we show the immobilization and label-free real-time *in situ* detection of live bacterial cells (*E. coli*) in 4-(2-hydroxyethyl)-1-piperazineethanesulfonic acid (HEPES) buffer, demonstrating qualitative and quantitative agreement in the mechanical response of three different resonance modes.

II. SENSORS

A. Design and fabrication

The devices used in this study are silicon cantilever arrays containing 15 to 18 sensors. The microfabrication process (Tyndall National Institute, Cork, Ireland) is based on three photolithography steps, schematically represented in Fig. 1. The fabrication starts from a silicon-on-insulator (SOI) wafer substrate, 100 mm in diameter, with a 7 μm Si layer on 2 μm SiO_2 (WaferPro LLC). A 5 μm plasma-enhanced chemical vapor deposition (PECVD) SiO_2 hard mask is deposited on the wafer backside and patterned via photolithography and dry etching [Figs. 1(a) and 1(b)] to defin the backside opening geometry. Subsequently, a 30 nm-thick stress-release SiO_2 layer is thermally grown on the wafer front, followed by 100 nm low pressure chemical vapor deposition (LPCVD) Si_3N_4 [Fig. 1(c)]. A second photolithography, followed by Si_3N_4 dry etching and SiO_2 wet etching in KOH, define the hinge region of the resonators [Fig. 1(d)]. Careful adjustment of wet etching conditions allows us to etch down 5 μm of the 7 μm silicon device layer, to achieve 2 μm-thick cantilevers. After Si_3N_4 and SiO_2 removal in wet solutions (hot H_3PO_4 and 10:1 HF, respectively), shown in Fig. 1(e), the resonator geometry is patterned via a third photolithography followed by silicon dry etching [Fig. 1(f)]. 100 nm aluminum is deposited via evaporation on the wafer front as a protective layer during the wafer-through dry silicon backside etching [Fig. 1(g)]. In this step, PECVD SiO_2 acts as a

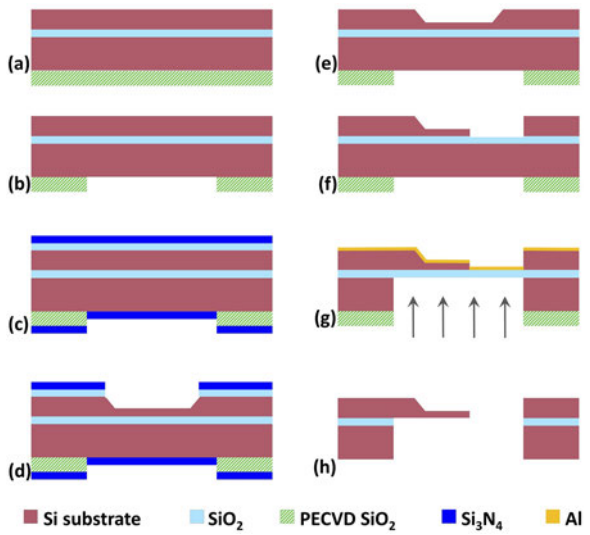

FIG. 1. Schematic representation of the fabrication process flo of the microcantilever sensors. A hard mask is deposited at the backside of a SOI substrate (a), followed by the patterning of the backside opening geometry and deposition of protective silicon nitride [(b) and (c)]. Resonator hinge [(d) and (e)] and profil (f) are define via two photolithographic steps. A protective layer is deposited on the wafer front in order to proceed with the backside wafer-through etching (g) and fina release in wet etching solutions (h). The wafer is shown in the cross section, with dimensions not to scale.

hard mask, while the buried SiO_2 is an etching stop layer. Resonators are finall released via Al and SiO_2 wet etching in BHF.

The fina devices consist of 15 cantilevers arrays (500 μm long, 95 μm wide, and 2.3 μm thick) and 18 cantilevers array (400 μm long, 70 μm wide, and 2.3 μm thick). Each wafer contains 308 chips, which can be easily detached with manual tweezers, thanks to cleavage lines define in the firs lithographic step. The hinge, patterned via the second photolithography, allows for precise definitio of the resonator length, which could otherwise vary among adjacent sensors, due to the isotropic release at the end of the fabrication process. In addition, the backside of every chip is patterned into a comb-like structure, which extrudes out of the chip body and serves to prevent cross contamination during capillary functionalization, as will be explained in Sec. II B. Figure 2 shows SEM images of a completed 18-microcantilever array chip, where the comb structure and a zoomed-in image on the hinge region are clearly visible.

The devices described in this paper are operated in dynamic mode, have a spring constant down to 0.4 N/m, and a mass down to 160 ng. However, thinner sensors have also been fabricated (1 μm thick) by increasing the KOH wet etching time in Fig. 1(e). Thinner cantilevers result in a lower spring constant (down to 0.03 N/m), more suitable for static mode operation where quasi-static deflectio is targeted.

B. Functionalization

One of the many advantages of using an array with multiple microresonators is the possibility to functionalize the surface of each cantilever with different specifi molecules.[1–3] This allows us to tackle multiple biorecognition events within the same experiment, maximizing the binding efficienc of target molecules, as well as enabling the passivation of some resonators to act as controls toward non-specifi binding. A differential readout between cantilevers in the array allows us to directly compare the binding efficienc of the same analyte to different molecules or receptors.

In order to prepare the sensors for functionalization, shortly before experiment, the chip is coated via metal evaporation (Temescal FC-2000, Scotech) with 3 nm of titanium, and 23/33 nm gold on the top and the bottom face, respectively. The different gold thickness between the cantilever top and the bottom side facilitates static mode operation.[25] Furthermore, the gold fil has the double function of (i) self-assembling and anchoring the functionalization molecules via a thiol group on the interface of the cantilevers and (ii) maximize surface reflectivit for optical detection.

We focus on two functionalization strategies, namely, glass microcapillaries and inkjet spotting, which are adapted to the newly implemented 15 and 18 sensor arrays.

1. Microcapillaries

Sterile and disposable glass microcapillaries (King Precision Glass, Inc.) are aligned with the cantilever array with the help of a custom-made platform that ensures fir clamping and micrometer precision movement in three directions (see Fig. S1). Resonators are then gently inserted into the microcapillaries, as shown in Fig. 3. For both designs of 15 and 18 sensors, the chip width is 3 mm, while the sensor pitch is 205 and 170 μm, respectively. Two different config urations are, therefore, adopted: 18 sensor chips are aligned with 9 capillaries with a 335 μm outer diameter (295 μm I.D.), so as to contain 2 sensors each, as shown in Fig. 3(a). 15 sensor arrays are aligned with a set of 5 capillaries with an outer diameter of 610 μm (570 μm I.D.) so that each capillary contains three cantilevers, as shown in Fig. 3(b).

In order to ensure full sensor functionalization, the hinge regions need to be fully covered by the microcapillaries. The comb structure at the backside of the wafer prevents the microcapillaries to reach the chip body, which would offer a cross contamination path between adjacent capillaries.[27] The back-end of microcapillaries is inserted in larger glass tubes (708744 Brand™ Blaubrand™ IntraMARK™, Fig. S1), which facilitate the solution injection by means of an automatic pipette and serve as reservoirs during incubation time, which typically ranges from a few minutes to 1 h.

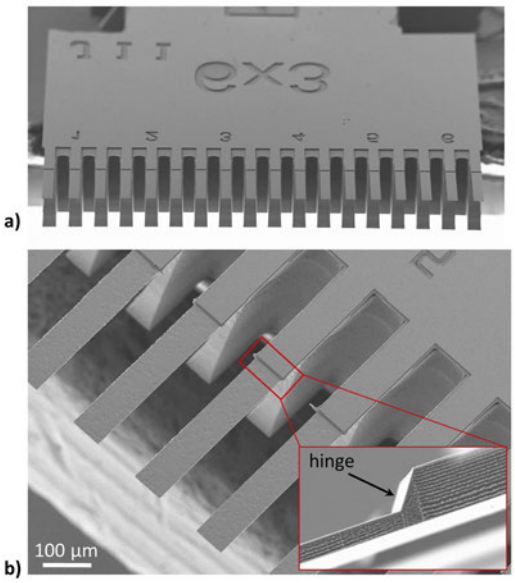

FIG. 2. (a) SEM image of a 18-sensor chip. Fabricated cantilevers are 400 μm long, 2.3 μm thick, and 70 μm wide. (b) Zoomed-in image of cantilevers. The inset shows a side view of the hinge region, which define the mechanical clamping point and, thus, the length (and resonance frequency) of the resonators. The comb-like structure close to the chip body is visible underneath the sensors. It extends between the chip body and the hinge, so as to prevent cross contamination while ensuring hinge covering during functionalization via capillaries.

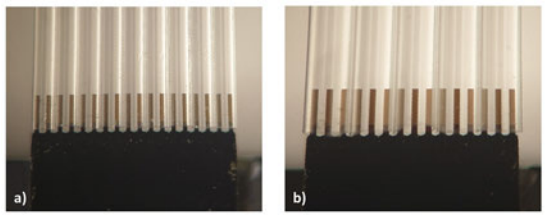

FIG. 3. Cantilever functionalization via immersion in glass microcapillaries. (a) 18 cantilever (170 μm pitch) chip aligned with 9 glass capillaries (295 μm I.D.). Each capillary contains two sensors. (b) 15 array (pitch 205 μm) chip aligned with 5 glass capillaries (570 μm I.D.). Each capillary contains three sensors.

The glass microcapillary technique minimizes cross contamination among adjacent sensors and allows us to fully immerse the resonators in solutions, so as to simultaneously and uniformly coat top and bottom surfaces. Solutions need to be injected one by one (about 10–30 μl per capillary), but this can be achieved rather quickly, minimizing the fillin delay between the firs and the last capillary to less than 2 min. Moreover, incubation time is easy to control. However, maximum attention needs to be paid during the microcapillary placement and clamping, in order to facilitate chip alignment and avoid sensor rupture. In addition, the solution must be injected in each reservoir via one continuous pumping step to promote the capillary flo toward the sensors and to avoid the formation of air bubbles.

2. Inkjet spotter

Inkjet spotting offers an alternative method for chip functionalization and is usually recommended for large devices or even for wafer-level functionalization.[27]

We use a MD-P-705-L inkjet dispensing system (microdrop Technologies GmbH) equipped with a three-axis micropositioning system that reaches an absolute ±5 μm accuracy. A piezo-driven glass autopipet (AD-K-501) with a 30–70 μm nozzle diameter allows us to dispense single droplets, corresponding to volumes between few tens to few hundreds of pl. A stroboscopic camera system allows visual monitoring of droplet ejection to control dimensions and prevent satellite droplets, via adjustment of piezo-voltages and pulse durations. The vertical separation between the nozzle and the substrate is typically 0.2–0.5 mm. Figures 4(a)–4(c) show the dispensing of water (60 V and 30 μs). Pictures are taken every 200 μs until complete droplet formation.

A software interface allows us to control pitch and number of ejected droplets on each sensor with ±1 μm repetition precision: selecting adequate parameters, droplets merge into a continuous layer covering one side of the entire cantilever length [Fig. 4(d)]. 18 sensors can be one-side coated in about 20 s with a single autopipet flui loading (max. 25 μl). Automated dispensing patterns can also be programmed (see Movie 1 in the supplementary material), by assigning offsets or definin matrix geometries, which is particularly useful to functionalize different sensors with different solutions. In the latter case, the autopipet must be thoroughly emptied and washed before loading a different solution, to avoid contamination. Moreover, in order to avoid cross contamination via evaporation, solutions need to be spotted in the order of decreasing volatility.[27]

With respect to microcapillaries, inkjet spotting is faster, allows us to minimize the liquid volumes, does not require manual alignment, and allows us to quickly create dispensing patterns on the target surface. The latter can be a key feature for specifi experiments, as both static and dynamic mode sensing are affected by surface stress,[28,29] receptor layer, and analyte binding locations.[15,30,31]

In addition, it is scalable to large arrays and can coat arbitrary structures in non-contact mode. The major limitation is the ability to coat only one side of the chip at the time. However, our custom-built chip holder allows for a quick manual fli upside down and repositioning. In addition, it is possible to wet both top and bottom surfaces of the cantilever by spotting the droplet closer to the lateral edge of the resonator (see Movie 2 of the supplementary material). Humidity inside the dispensing area and chip temperature

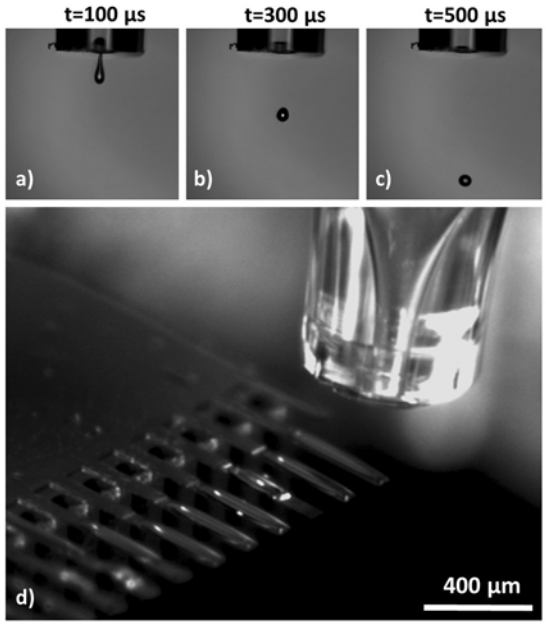

FIG. 4. Cantilever functionalization via inkjet spotting. [(a)–(c)] water droplet ejection at 60 V and 30 μs pulse. The stroboscopic camera allows visualization every 200 μs, showing that the droplet is fully formed after 500 μs from ejection. (d) Video control of the inkjet nozzle aligned with the cantilever array. The vertical separation between the nozzle and the substrate is typically 0.5 mm. An array of 18 cantilevers can be one-side coated in less than 20 s.

are critical parameters on which both incubation/functionalization time and steady solution concentration depend. We read humidity levels with a commercial sensor (Inkbird IHC-200) placed in close proximity to the chip and adjust humidity (usually 70% relative humidity) via a custom-made water nebulizer vapor injection system connected to compressed air. The chip temperature is regulated through a feedback control system integrated within the spotter equipment, in order to keep sensor surfaces at the dew point temperature.

III. TRANSDUCTION

Cantilever arrays are mounted into a microfluidi measurement chamber, micromachined in polyether ether ketone (PEEK) and previously described in Ref. 23. Briefly the chamber serves to mechanically clamp the chip and to immerse it in a 6 μl microfluidi volume, for in-liquid measurements. Microfluidi inlets and outlets connect the chamber to a fluidi line, software-controlled via a system of solenoid valves (ASCO Valve, Inc.) and automated syringes (Kent Scientifi Corporation, Lee Company), which enables nl to ml injection volumes and exchange of multiple samples during experiments.[23] In order to ensure temperature stability and insulation, the whole setup (including fluidi pumps and tubings) is enclosed in a thermally insulated box. The platform box is designed as a modular aluminum frame with foil-faced, polyisocyanurate (PIR) rigid insulation boards (Ballytherm Ltd.). The internal temperature is regulated via meandering water line floo heating and a fine-tune

proportional–integral–derivative (PID) feedback thermal circulator control system (Peter Huber Kältemaschinenbau AG), resulting in stable internal temperature with 0.02 °C precision.[32]

Dynamic mode operation is achieved via a custom-built piezoceramic stack actuator, placed in a pocket underneath the chip and isolated from the fluidi volume by using a 200 μm-thick PEEK membrane.[23] Mechanical signals are detected via an optical beam deflectio (OBD) readout,[33] able to detect cantilever oscillation with sub-nanometer resolution.

A. Piezo-stack actuator

Due to geometry and frequency range requirements, the piezo-stack actuator is assembled in-house from commercial piezoelectric sheets (Noliac, *CTS*).

Given the flui around the resonators and the presence of a PEEK membrane between the actuator and the chip, large displacement and good mechanical coupling are key requirements for efficien actuation. The selected actuator material is NCE51, a soft-doped piezoelectric ceramic, characterized by high electromechanical coupling factors that result in large induced deflections [34] NCE51 piezoelectric sheets with screen printed Ag electrodes on opposite sides are diced into $2 \times 2\,mm^2$ and $3 \times 2\,mm^2$ chips and bonded face-to-face via conductive epoxy glue (EPO-TEK® E4110; Epoxy Technology, Inc.). Copper bus wires (0.1 mm diameter, 0822942, BLOCK Transformatoren-Elektronik GmbH) are glued to the diced chips with viscous conductive epoxy resin (EPO-TEK EJ2189) and are used to electrically connect same-polarity faces of adjacent stacked chips (Fig. 5). Longer wires (0.22 mm diameter, 918811, BLOCK Transformatoren-Elektronik GmbH) are attached at the outer surfaces of the stack and constitute the main electrical connections to apply driving voltage (<5 V) to the actuator. A thicker layer of soft non-conductive epoxy glue (EPO-TEK 301) is evenly distributed with a fin brush around the short wires and the full body of the actuator, in order to confer robustness to the whole structure while not constraining its vibration.[35] The stack actuator is mounted into the pocket underneath the chip and glued to the PEEK membrane with a thin layer of two-component hard epoxy glue (Torr Seal®, Kurt J. Lesker Company). At the backside of the piezo-stack actuator, a $15 \times 10 \times 2\,mm^3$ glass ceramic plate (MACOR, Radionics Ltd.) serves as a mechanical reflecto and is used to apply a gentle pressure toward the actuator, thus maximizing the mechanical coupling between the piezo-actuator and the cantilever chip. The measurement chamber is then closed with a Peltier element and a metallic plate tightly screwed to the PEEK body.

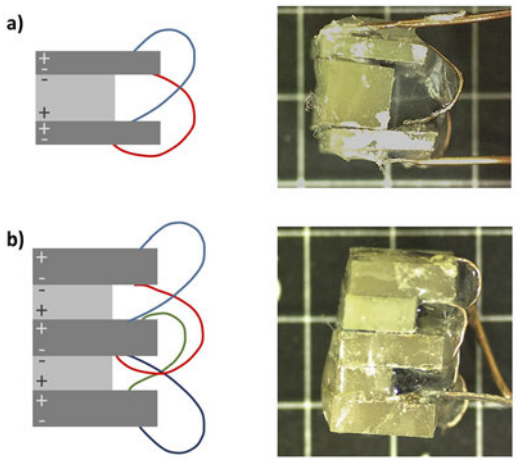

FIG. 5. Custom-made piezoelectric actuator stacks for dynamic mode operation of cantilever arrays. Three-stack [(a), t = 0.5/1/0.5 mm] and five-stac [(b), t = 1/1/1/1/1 mm] actuators have been built by gluing commercial piezoceramic chips and providing electrical interconnections via bus wires. All actuators successfully allow the operation of microcantilevers up to 2 MHz, with a voltage actuation between 1 and 5 V. External connections are applied to the outer surfaces of the stack to provide driving voltage.

By combining multiple piezoceramic chips, the resulting stack is able to achieve a larger displacement than the one of a single chip, while maintaining a low drive voltage range and sub-millisecond response times.[36] Three- and five-stac actuators have been fabricated, also varying the single layer thicknesses, as shown in Fig. 5. However, when comparing different configurations three-stack devices show larger induced displacements on the PEEK membrane with respect to five-laye stacks (see Fig. S2). We believe that this is due to fabrication variability, as a result of the manual process of gluing and aligning wires and piezoelectric chips. However, all fabricated actuators show successful and comparable performances: once integrated in measurement chambers, cantilever resonance modes were detected up to 2 MHz, given actuation voltages between 1 and 5 V (see Fig. S3).

B. Optical detection system

The mechanical oscillation of microcantilever sensors is detected via an OBD readout.[33] A laser diode beam (830 nm, 10 mW; Thorlabs Ltd.) is focused close to the tip of cantilevers and reflecte back to a two-cell photosensitive detector (PSD, S5870, Hamamatsu Photonics K.K.). The laser is mounted on an optical cage, previously described in Refs. 23 and 32, which contains optical elements to collimate and focus the beam with a radius of about 7 μm on the reflectiv cantilever gold surface.

Key requirement to use cantilevers as sensors is the precise positioning of the laser toward the tip of the cantilevers and on the flexura node for optimal oscillation amplitude detection. To do so, the optical cage hosting the laser is moved by a system of four microtranslation stages, two manual and two electric [M-122.2DD and M-110.1DG Physik Instrumente (PI) GmbH & Co. KG]. This micropositioning system allows us to focus the laser spot across the array with two-axis micrometer precision to sequentially scan all sensors (horizontal x range: 5 mm range with 50 nm precision; vertical y range: 25 mm with 100 nm precision). At first the laser spot is coarsely placed close to the firs cantilever of the array to perform an automated full array scan (a detail in Fig. 6). Subsequently, a fine scan allows us to identify and store the optimal nodal point coordinates per resonator, through the dedicated home-built LabView module (National Instruments): each device is actuated while the laser position is adjusted with micrometer precision close to the resonator free end, so as to fin the coordinates that maximize the vibrational amplitude. Scanning the chip area not only allows the optimal and consistent positioning of the laser on the sensors but also provides a quality control of the array itself.

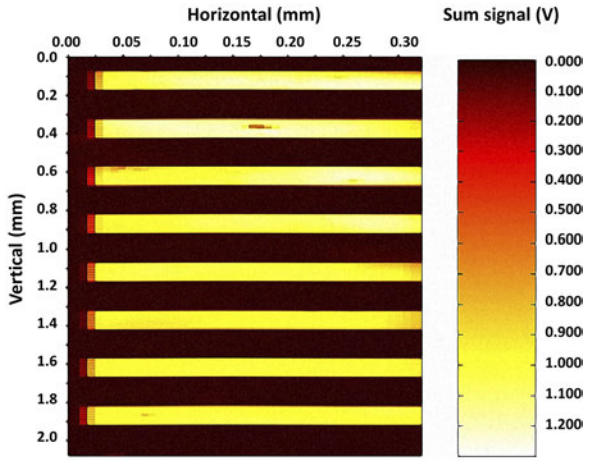

FIG. 6. Intensity plot of the PSD sum signal across one portion of the cantilever array. The step size of the laser scan is 8 μm. The sum plot allows us to place the laser toward the front end of each sensor on the optimal flexura node position. Note that the cantilever array is not perfectly orthogonal, and this slight tilt can be evaluated and compensated via the automatic XYZ laser positioning system.

The microcantilever oscillation causes a shift in the position of the reflecte beam on the $10 \times 10\ \text{mm}^2$ two-cell PSD (S5870, Hamamatsu Photonics K.K.). PSD current signals from the two optical sensor cells are converted into voltage and combined into sum and differential signals through a custom-made electronic amplificatio circuit[35] (see Fig. S4). The sum signal corresponds to the intensity of the incident laser on the full PSD surface, while the differential voltage relates to the position of the reflecte laser spot and, thus, is modulated by cantilever oscillation. The two PSD output signals are firs amplifie and filtere through a low-noise preamplifie (SR560, Stanford Research Systems) and later acquired at 60 MSa/s by using an oscilloscope card (PCI-5105, 60 MHz bandwidth, 12-bit resolution; National Instruments).

The PSD is biased with a home-built power supply (±15, +5 V) that features built-in overload protection and minimizes the noise floo power spectrum.[37] The selected PSD has a rise time of 100 ns, which results in a maximum detectable frequency of 10 MHz. However, the actual optical readout bandwidth is limited by the custom-made I–V converter electronic circuit. Operational amplifier (LT1361, Analog Devices, Inc.) and the RC filte stage (5.6 kΩ and 2.2 pF) have been selected so as to guarantee linear and fast optical detection up to few MHz, thus enabling the tracking of higher resonance modes.[29] Indeed, the readout system, considering the PSD and electronic I–V converter circuit, has a fina cutoff frequency of 4.8 MHz and a gain of 1, calculated according to Ref. 38.

Considering the full transduction scheme, the upper limit of the current measurement bandwidth is set by the actuation stage, as the operational frequency of the piezo-stack actuator reaches a maximum of 2 MHz (Figs. S2 and S3).

IV. PHASE-LOCKED LOOP IMPLEMENTATION

The established method for mechanical response detection of cantilever arrays in liquid, with up to eight sensors, consists of carrying out a frequency sweep analysis around the resonance modes of each device.[5,23] A continuous sweep scan across the array allows us to track the real-time evolution of the amplitude and phase responses of the oscillating structures, experimentally determined as explained in Ref. 6, while samples and analytes are injected in the measurement chamber and bind to the sensitized resonators. This method has demonstrated a mass resolution down to 10 pg and a time resolution (time interval between two consecutive measurements on the same cantilever) of about 20 s, when tracking three resonance modes of eight sensors.[7]

In this manuscript, we implement a new method that allows us to extend the measurement capability to as many sensors as needed (18 in the newly developed arrays), without losing temporal resolution and while improving the sensing performance by more than sevenfold. A proportional–integral–derivative (PID) controlled phase-locked loop (PLL) is built via an in-house developed LabVIEW (National Instruments) code, directly interfaced with the experimental hardware and able to track up to 4 modes of 18 sensors in parallel over several hours.

Before experiment, the cantilevers are mounted in the microfluidic chamber and immersed in a buffer solution to stabilize for up to 2 h. After this equilibration step, a frequency sweep is performed for each cantilever and resonant mode to determine the optimal phase shift (between the driving signal and the response signal) that maximizes the resonant motion amplitude. To do so, a harmonic signal is produced by a waveform generator card (PCI-5406, 40 MHz bandwidth, 16-bit resolution; National Instruments) and sent to both the piezo-stack actuator and a high-speed data acquisition card (PCI-5105, 60 MHz bandwidth, 12-bit resolution; National Instruments). A custom-written LabVIEW program (NI-TClk Synchronization VIs) enables picosecond synchronization between the drive and acquisition cards, connected via a RTSI bus cable.

Subsequently, the PID parameters are evaluated through the Ziegler–Nichols auto-tuning method:[39] each cantilever is excited to an arbitrary frequency (typically ±1 kHz of the selected resonant frequency), while the phase responses are recorded and used by the auto-tuning algorithm to determine the fine-tune PID parameters for each sensor. Note that selecting an excitation frequency shift close to the one expected for the specifi experiment yields the best PID parameters.

Finally, the piezo-stack actuator sequentially drives each cantilever around its nominal resonance frequency for a few ms, while the phase responses are separately acquired. The optimized PID parameters are used to compute the adjustment to the driving frequency that maintains the phase of each device constant (locked) at resonance. The PID computation of the frequency is performed simultaneously for all sensors, thus allowing for up-scaling to as many cantilevers and as many resonant modes as needed. In a typical experiment, four resonant modes and 18 cantilevers are measured, resulting in 72 parallel PID controllers. If the system is ideally unperturbed, the frequency that locks the phase (resonant frequency) would remain constant, but upon perturbation (e.g., mass adsorption and temperature or flui density changes), the frequency will shift accordingly. The time between the collection of two consecutive frequency measurements when the laser is kept on one sensor is 80 ms (1 ms acquisition, 10 MSa/s). However, when scanning the full array of 18 sensors, the time delay between two consecutive measurements on the same cantilever is in the order of few seconds

(below 15 s for 18 cantilevers and four resonance modes) and is mainly due to physical stage movement. Such an interval does not constitute a limitation for our experiments, as the time range of interest for biological event detection within our setup lies in the order of few minutes, as shown in Sec. VI of this manuscript.

V. DETECTION LIMIT AND NOISE

The binding of target molecules on the sensitized surface of cantilevers induces a frequency shift that can be converted into mass uptake Δm via the following equation [24,26] (see the supplementary material for more details):

$$f_{r,n} = \beta_n \sqrt{\frac{k}{m_c + \Delta m + m_f \Gamma_r^f(Re_n, \kappa_n)}}, \tag{1}$$

where $f_{r,n}$ is the resonance frequency of the n-th mode of vibration, $m_f = \rho_f \pi b^2 L/4$ is the flui mass load on the cantilever, calculated as the mass of a flui cylinder with the radius equal to half the cantilever width b, $\Gamma_r^f(Re, \kappa_n)$ is the real component of the hydrodynamic function and depends on flui properties through the Reynolds number Re and on the normalized mode number κ_n, $\beta_n = \alpha_n^2/(2\pi\sqrt{3})$, α_n being the n-th positive root of $1 + \cos\alpha_n \cosh\alpha_n = 0$, from the Euler Bernoulli beam theory, and k and m_c are the cantilever stiffness and mass, respectively.

Equation (1) needs an accurate knowledge of flui density and viscosity over the full experiment duration, in order to precisely compute the hydrodynamic function values. We previously introduced an accurate approximation of the hydrodynamic function over large Reynolds numbers.[24] However, in a differential analysis, the average frequency shift of a set of sensors (typically functionalized with the same molecules) is evaluated with respect to another set on the same array (either control sensors or devices with a different functionalization). By doing so, accurate knowledge of fluidi properties over the whole experiment is no longer required, and the differential mass uptake between the two sets of sensors can be derived from Eq. (1) and written as follows (see the supplementary material):

$$\Delta m_1 - \Delta m_2 = k\beta_n^2 \left(\frac{1}{f_{1,n}^2} - \frac{1}{f_{2,n}^2} \right), \tag{2}$$

where $f_{1,n}$ and $f_{2,n}$ are the resonance frequencies of cantilevers (or average resonance frequency of cantilever sets) 1 and 2. This not only allows us to be independent of environmental variations (e.g., temperature and flui viscosity) but also allows us to directly compare the binding efficienc of the same analyte toward different chemistries in the same time frame and under identical experimental conditions.

The mass resolution δm_n relative to the n-th mode of resonance, under the assumption of small added mass, can be written as follows (see the supplementary material):

$$\delta m_n = -2 \frac{\delta f_n}{f_{r,n}} m_c, \tag{3}$$

where δf_n is the frequency noise.

The normalized frequency noise $\delta f_n/f_{r,n}$ can be evaluated computing the Allan deviation of the frequency $\sigma_A(\tau)$, define as the statistical variance of N measured normalized frequency values $y(t)$ over an average time τ, as as follows:[40]

$$\sigma_A(\tau) = \sqrt{\sigma_A^2(\tau)} = \sqrt{\frac{1}{2(N+1)} \sum_{i=1}^{N} (y_{i+1,\tau} - y_{i,\tau})^2}. \tag{4}$$

Figure 7 shows the typical Allan deviation plot of the fift flexu ral mode of a microcantilever sensor in PBS, stabilized at 26 °C, and allows us to identify the noise contributions in our measurement system. Higher modes of vibration, between 300 kHz and 1.5 MHz, are normally considered due to larger responsivity to mass uptake[29] and compatibility to our measurement setup. Frequency points are collected while keeping the laser spot on one single sensor, acquiring at 10 MSa/s sample rate for intervals of 1 ms, with a time resolution of 80 ms. $\sigma_A(\tau)$ allows us to directly estimate the mass sensitivity of the system, via Eq. (3), and to recognize the most typical noise contributions. The left part of the plot, below 10 s of integration time, can be calculated as follows, assuming white noise behavior[41] (thin blue line in Fig. 7):

$$\sigma_A(\tau) = \frac{\delta f}{f_{r,n}} = \frac{1}{2Q_n} \frac{N}{S} \sqrt{BW}, \tag{5}$$

where Q_n is the quality factor of the considered resonance mode, N is the noise level measured as the square root of the power spectral density around resonance (LabVIEW, FFT Power Spectrum, and PSD VI) in $V/\sqrt{Hz}$, S is the amplitude of the output signal detected via a PSD in V, and BW is the measurement bandwidth, define as $1/\tau$. The measured data lie in the same range of the theoretical estimated limit; however, they exhibit different scaling laws with respect

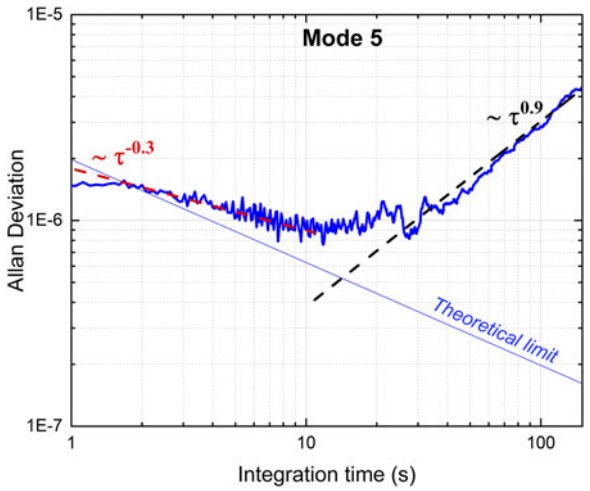

FIG. 7. Allan deviation plot for one sensor immersed in PBS stabilized at 26 °C. The left asymptote of the AD plot is in good agreement with the theoretical limit, calculated from power spectral density measurement, as shown in Eq. (5). It scales as $\tau^{-0.3}$, indicating that low integration times are not dominated by white noise (which typically scales as $\tau^{-0.5}$). The system noise is dominated by a thermal drift after an integration time of about 10 s. The main source of frequency noise in our biological experiments (i.e., binding molecules to receptors placed on a sensor surface) is, therefore, the thermal drift, considering that biological processes occur in a time range in the order of tens of seconds to minutes.

to the integration time τ. Below 10 s, $\sigma_A(\tau)$ scales as $\tau^{-0.3}$ (red fi in Fig. 7), indicating that low integration times are not dominated by white noise (e.g., thermomechanical noise), which typically scales as $\tau^{-0.5}$.

Flat $1/f$ noise contribution ($\sim\tau^0$) is visible around 10 s, while larger integration times are dominated by the system thermal drift ($\sim\tau^\alpha$, with $0.5 < \alpha < 1$), as shown in black dashes in Fig. 7.

Measuring at 10 s integration time ensures the lowest noise level and, thus, the best mass resolution, down to 0.3 pg according to Eq. (3). However, the relevant time range for biological molecular detection normally corresponds to several minutes, due to analyte diffusion kinetics and transient binding to the resonators, which depend both on the sample concentration and target molecule size. The thermal drift, thus, represents the main source of noise in our experimental conditions.

In order to compare the sensing performance of the PLL method to the previous frequency sweep strategy (sweep method), a 15-cantilever array is loaded in the measurement chamber fille with PBS. After a stabilization of 2 h at 26 °C, frequency data are acquired for 30 min via the sweep method and immediately after for 30 min via the PLL. The 10 min standard deviation of resonance frequency for ten cantilevers is measured three times over the data collection. The average frequency standard deviation of the array over a time window of 10 min is 39 ± 5 and 6 ± 1.5 Hz for sweep and PLL, respectively, considering mode 5. 30 ± 4 and 4 ± 2 Hz for sweep and PLL, respectively, were obtained for mode 6 (see Fig. S5 and Table S1). The PLL improves the frequency noise by up to a factor of 7 with respect to the sweep method. We, thus, estimate the same improvement in terms of mass resolution, thus pushing down to about 2 pg the detection limit of 10 pg, previously reported for sweep analysis.[7] In addition, the PLL method is faster than the sweep, allowing to improve the time resolution by more than a factor of 3: consecutive frequency measurements were collected every 20 s via sweep and every 6 s with PLL, when considering the same number of sensors and resonance modes (Table S1).

We also investigate the effect of different surface chemistry on the resonators, via the capillary functionalization with hydrophilic (aliphatic thiol molecules terminated with COOH, PEG, or NH_2 groups) and hydrophobic (aliphatic thiol molecules terminated with the CH_3 group) self-assembled monolayers (Fig. S6). No substantial effect on the frequency noise was observed, independent of the chemical functionalization. The Allan deviation ranges in the same order of magnitude with less than a factor of 3 difference (Fig. S6). This is a positive finding as microcantilevers are regularly functionalized with different chemicals in order to immobilize proteins with high binding efficiency In addition, the resonance modes considered (fift to eighth, corresponding to frequencies between 450 and 1200 kHz) show Allan deviation differences by less than a factor of 4. Mode 6 exhibits the best performance, achieving frequency stability down to 10^5 considering an integration time of 5 min, which is equivalent to an estimated mass resolution of 3 pg, when considering Eq. (2) [Figs. S6(a) and S6(c)].

A. Bacteria detection

To demonstrate multimodal quantitative biological measurements with the new developed devices and system, we detect living bacteria binding on the surface of functionalized gold-coated cantilevers.

An array of 18 sensors (400 × 2.3 × 70 μm^3) is functionalized via the glass microcapillary method. Cantilevers are split into four groups, evenly distributed across the array and incubated for 10 min in 2 mM ethanol-based solutions of self-assembling thiol molecules terminated with CH_3, NH_2, PEG, and COOH groups (see the supplementary material for detailed description). The chip is subsequently rinsed in pure ethanol for 10 min, nanopure water for 5 min, and stored overnight in HEPES buffer (pH = 7; Sigma-Aldrich) at 26 °C. The following day, the measurement box enclosing the full setup and fluidi samples is thermally stabilized at 26 °C. Finally, the chip is mounted in the HEPES-fille measurement chamber and left for stabilization for 2 additional hours.

E. coli bacterial cells (XL10-Gold® Ultracompetent Cells, Agilent) are revived from frozen stock via overnight incubation at 37 °C and 180 rpm in a Luria–Bertani (LB) broth (Sigma-Aldrich). During machine priming and thermalization, 1 ml of overnight bacteria solution is inoculated in 10 ml fresh LB. The bacterial growth protocol is timed to have fresh cells in the exponential growth phase to be injected into the microfluidi chamber. While the PLL tracks resonance frequencies in HEPES buffer, the cells are resuspended in HEPES buffer at 26 °C and diluted to 10^6 cells/μl. The bacteria solution is loaded in the automated syringe pump and pushed up to the valve-controlled fluidi inlet of the measurement chamber. By doing so, the bacteria solution has about 40 min to equilibrate at 26 °C before direct injection onto the resonators (100 μl @ 50 μl/min).

PLL tracking is set up for 15 cantilevers (three sensors broke during manual handling of the chip) and four modes of resonance. Frequency values are acquired at 10 MSa/s for 1 ms every PLL cycle, with a resulting time resolution of 11 s. Frequency data are collected for 1 h in HEPES buffer and for 40 min after injection of bacterial cells into the microfluidi chamber.

Figures 8(a)–8(c) show the time evolution of the average resonance frequencies of cantilevers with analogous functionalization, for three modes of resonance, as bacteria are injected into the chamber, at t = 0. As can be seen, resonance frequencies start decreasing immediately after bacteria injection and reach a plateau after about 10 min. Sensors functionalized with COOH and NH_2 exhibit the largest frequency shift, thus mass uptake, while PEG-functionalized cantilevers undergo the lowest frequency variation. This can be explained with the presence of charges on COOH and NH_2 functional groups, which interact with the charged bacteria membranes, resulting in a weak but effective ionic immobilization.

Conversely, PEG does not exhibit free charges and is normally used as a passivation layer, to act as control toward non-specifi binding.[42]

Differential mass uptakes are calculated according to Eq. (2) with respect to PEG sensors, which are used as reference devices, as shown in Figs. 8(d)–8(f). The three modes confir the same qualitative and quantitative behavior: in all cases, a differential mass uptake between 1.5 and 1.9 ng is observed for NH_2 sensors, between 1 and 1.3 ng for COOH sensors, 30 min after bacteria injection. Differential analysis allows removing the effect of non-specifi binding, visible in the PEG-functionalized control cantilevers, as well as any global drift in the system (e.g., temperature variations). Interestingly, we observe that in bacteria solution, the frequency noise increases up

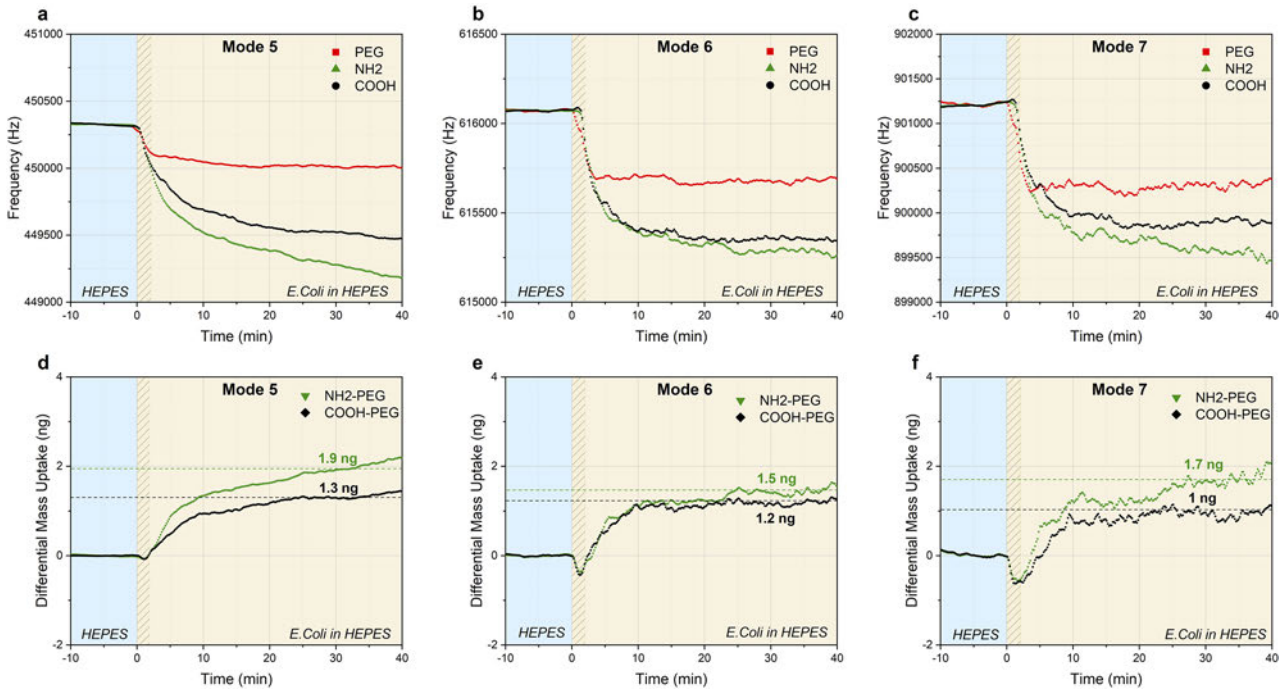

FIG. 8. Live bacteria detection via PLL tracking of the three resonant modes of 15 cantilevers (400 × 2.3 × 70 μm^3). Per each mode considered, the resonance frequency of sensors with the same functionalization is averaged and plotted over time [(a)–(c)]. Sensors are firs stabilized and measured for 1 h in HEPES buffer at 26 °C (collapsed reference traces, below t = 0). Bacteria injection (10^6 cells/μl) in the microfluidi chamber at t = 0 (dashed orange region) causes a shift in resonance frequency due to bacteria attachment and subsequent mass loading on the sensor surface. NH_2 and COOH exhibit the largest frequency shift, due to the charge interaction between bacterial membranes and functionalization groups. [(d)–(f)] Differential mass uptake with respect to the PEG reference sensors is calculated for the three modes. Dashed lines indicate the mass uptake in ng after 30 min from bacteria injection. The three modes show comparable qualitative and quantitative results, confirmin the robustness of the implemented measurement method.

to a factor of 4 with respect to levels in buffer, when considering the average of the frequency standard deviation over a time window of 10 min (Fig. S7). We attribute this phenomenon to the increase in optical noise due to laser scattering caused by bacterial cells moving and floatin in the measurement chamber.

Under such conditions, the equivalent mass noise increases from few pg up to 60 pg. Given that the bacterial mass uptake is in the order of few nanograms, as seen in Figs. 8(d)–8(f), this noise increase does not limit our experiment. In addition, when considering the detection of smaller analytes such as proteins[7] or DNA fragments,[10] a noise increase after sample injection has never been observed, probably due to the fact that such analytes belong to a much lower size range and, thus, do not affect the optical laser path to and from the resonators.

VI. CONCLUSIONS

We report on the development of a nanomechanical measurement system, which allows the real-time detection of living cells via the tracking of up to 18 cantilevers and up to four resonance modes, simultaneously. With respect to previous publications, this work demonstrates more than three times faster and up to seven times more sensitive detection of larger arrays of microcantilevers in liquid. Such an achievement is the result of upscaling of the chip fabrication, from eight to 18 sensors per chip, along with the optimization of an optical detection readout and the implementation of the PLL method as the measurement strategy.

Sensor arrays are fabricated via standard cleanroom technology. A custom-built piezo-stack actuator is fabricated and allows us to drive resonators in liquid up to 2 MHz, while a commercial PSD is integrated in an in-house developed electronic readout system.

We implement the PLL measurement method, which allows us to track up to 18 × 4 mechanical signals over several hours, with a time resolution below 15 s. For each sensor, the PLL generates a closed feedback loop that allows us to drive the cantilevers close to resonance, while tracking the real-time evolution of the resonance frequency. Frequency noise analysis of the new devices and setup shows that, in the relevant time range for biological events (few minutes), the main noise contribution is the system thermal drift. When compared to the previous sweep method, routinely implemented for eight cantilever arrays, the PLL exhibits better sensing performance and faster operation. For the four modes considered (fift to eighth, corresponding to frequencies between 450 and 1200 kHz), Allan deviation analysis allows us to estimate a mass resolution down to 2 pg at 5 min integration times.

In addition, we show that measurement performance is not heavily affected by sensor surface chemistry. We report less than a factor of 3 difference in frequency noise of sensors with four

different functionalization groups (CH_3, PEG, NH_2, and COOH), resulting in an estimated mass resolution between 2 and 12 pg.

We demonstrate the mass uptake detection of living bacterial cells of the species *E. coli*, immobilized on the sensor surface via weak charge interaction. The three studied modes of resonance exhibit same qualitative and quantitative results, demonstrating the robustness and consistency of our method.

SUPPLEMENTARY MATERIAL

See the supplementary material for more details on capillary functionalization, self-assembled monolayer formation protocols, piezo-stack actuator characterization, and PSD electronic readout. A performance comparison between the sweep method and the PLL method is also provided, along with noise characterization for different modes and interface chemistries. Finally, a theoretical derivation of Eqs. (1)–(3) is provided. High-speed videos of inkjet droplet functionalization are also included.

ACKNOWLEDGMENTS

This work received funding from the European Union's Horizon 2020 research and innovation program under Grant Agreement No. 654384. This work was also supported by the Science Foundation Ireland under the IvP scheme (No. SFI/15/IA/3023), the CSET scheme (Grant No. SFI/10/CSET/B1821), and the SFI Research Infrastructure—Opportunistic Funding (Grant No. 16/RI/3403). The authors thank Alan Blake and co-workers from the Tyndall National Institute (Cork, Ireland) for fabricating the cantilever microchips, Neal O'Hara from the CRANN cleanroom facilities at TCD for the support in the Ti/Au evaporation, Hector Cavazos from ADAMA Innovations Ltd. (Ireland) for the multiple inputs during the fabrication process design, Patrick Murphy from the Mechanical Workshop at TCD for manufacturing the microfluidi chambers, Andreas Tonin from the University of Basel for the invaluable support in the design of the PSD electronic circuit and power supply, Professor Matthias Möbius from TCD for the support in high-speed video recording of inject spotting on cantilevers, and Dr. Tom Larsen from SerEnergy A/S (Denmark) and Professor Luis Guillermo Villanueva from École Polytechnique Fédérale de Lausanne for the fruitful discussions on PLL theory and Allan deviation analysis. SEM imaging was carried out at the CRANN Advanced Microscopy Laboratory (AML www.tcd.ie/crann/aml/).

DATA AVAILABILITY

The data that support the finding of this study are available from the corresponding author upon reasonable request.

REFERENCES

[1] A. Boisen, S. Dohn, S. S. Keller, S. Schmid, and M. Tenje, Rep. Prog. Phys. **74**, 036101 (2011).
[2] H. P. Lang, M. Hegner, and C. Gerber, in *Springer Handbook of Nanotechnology*, edited by B. Bhushan (Springer, Berlin, Heidelberg, 2010), p. 427.
[3] D. Liu and W. Shu, Curr. Org. Chem. **15**, 477 (2011).
[4] J. Fritz, M. K. Baller, H. P. Lang, H. Rothuizen, P. Vettiger, E. Meyer, H. J. Güntherodt, C. Gerber, and J. K. Gimzewski, Science **288**, 316 (2000).
[5] T. Braun, V. Barwich, M. K. Ghatkesar, A. H. Bredekamp, C. Gerber, M. Hegner, and H. P. Lang, Phys. Rev. E **72**, 031907 (2005).
[6] F. Padovani, J. Duffy, and M. Hegner, Nanoscale **9**, 17939 (2017).
[7] G. Brunetti, F. Padovani, A. De Pastina, C. Rotella, A. Monahan, S. L. Hoffman, S. A. Jongo, S. Abdulla, G. Corradin, G. Pluschke, C. Daubenberger, and M. Hegner, Nanoscale **13**, 2338 (2021).
[8] J. Zhang, H. P. Lang, F. Huber, A. Bietsch, W. Grange, U. Certa, R. McKendry, H.-J. Güntherodt, M. Hegner, and C. Gerber, Nat. Nanotechnol. **1**, 214 (2006).
[9] R. Mishra and M. Hegner, Nanotechnology **25**, 225501 (2014).
[10] J. Duffy, F. Padovani, G. Brunetti, P. Noy, U. Certa, and M. Hegner, Nanoscale **10**, 12797 (2018).
[11] S. B. Patil, R. M. Al-Jehani, H. Etayash, V. Turbe, K. Jiang, J. Bailey, W. Al-Akkad, R. Soudy, K. Kaur, R. A. McKendry, T. Thundat, and J. W. Ndieyira, Commun. Biol. **1**, 175 (2018).
[12] G. Longo, L. Alonso-Sarduy, L. M. Rio, A. Bizzini, A. Trampuz, J. Notz, G. Dietler, and S. Kasas, Nat. Nanotechnol. **8**, 522 (2013).
[13] K. Y. Gfeller, N. Nugaeva, and M. Hegner, Appl. Environ. Microbiol. **71**, 2626 (2005).
[14] N. Nugaeva, K. Y. Gfeller, N. Backmann, M. Düggelin, H. P. Lang, H.-J. Güntherodt, and M. Hegner, Microsc. Microanal. **13**, 13 (2007).
[15] N. Maloney, G. Lukacs, J. Jensen, and M. Hegner, Nanoscale **6**, 8242 (2014).
[16] E. Engvall and P. Perlmann, Immunochemistry **8**, 871 (1971).
[17] See https://www.biolinscientific.com/qsens for QSense Biolin Scientific
[18] D. G. Myszka, Anal. Biochem. **329**, 316 (2004).
[19] A. De Pastina and L. G. Villanueva, J. Micromech. Microeng. **30**, 043001 (2020).
[20] K. Länge, B. E. Rapp, and M. Rapp, Anal. Bioanal. Chem. **391**, 1509 (2008).
[21] G. Yoshikawa, T. Akiyama, S. Gautsch, P. Vettiger, and H. Rohrer, Nano Lett. **11**, 1044 (2011).
[22] J. L. Arlett, E. B. Myers, and M. L. Roukes, Nat. Nanotechnol. **6**, 203 (2011).
[23] M. Walther, P. M. Fleming, F. Padovani, and M. Hegner, EPJ Tech. Instrum. **2**, 7 (2015).
[24] F. Padovani, J. Duffy, and M. Hegner, Anal. Chem. **89**, 751 (2017).
[25] H. P. Lang, M. Hegner, and C. Gerber, in *Applied Scanning Probe Methods IV: Industrial Applications*, edited by B. Bhushan and H. Fuchs (Springer, Berlin, Heidelberg, 2006), p. 183.
[26] C. A. Van Eysden and J. E. Sader, J. Appl. Phys. **101**, 044908 (2007).
[27] A. Bietsch, J. Zhang, M. Hegner, H. P. Lang, and C. Gerber, Nanotechnology **15**, 873 (2004).
[28] M. J. Lachut and J. E. Sader, Appl. Phys. Lett. **95**, 193505 (2009).
[29] M. K. Ghatkesar, V. Barwich, T. Braun, J.-P. Ramseyer, C. Gerber, M. Hegner, H. P. Lang, U. Drechsler, and M. Despont, Nanotechnology **18**, 445502 (2007).
[30] S. Dohn, R. Sandberg, W. Svendsen, and A. Boisen, Appl. Phys. Lett. **86**, 233501 (2005).
[31] D. Ramos, M. Arroyo-Hernández, E. Gil-Santos, H. Duy Tong, C. Van Rijn, M. Calleja, and J. Tamayo, Anal. Chem. **81**, 2274 (2009).
[32] F. Padovani, Ph.D. thesis, School of Physics, Discipline of Physics, Trinity College Dublin, 2018.
[33] G. Meyer and N. M. Amer, Appl. Phys. Lett. **57**, 2089 (1990).
[34] See http://www.noliac.com/products/materials/nce51/ for information on piezo-ceramics material specifications
[35] M. Walther, Ph.D. thesis, School of Physics, Trinity College, Dublin, Ireland, 2015.
[36] S. Takahashi, Jpn. J. Appl. Phys., Part 1 **24**, 41 (1985).
[37] F. Wruck, Ph.D. thesis (School of Physics, Discipline of Physics, Trinity College Dublin, 2016).
[38] T. Fukuma, Rev. Sci. Instrum. **80**, 023707 (2009).
[39] J. G. Ziegler and N. B. Nichols, J. Dyn. Sys., Meas., Control. **115**, 220 (1993).
[40] S. Schmid, L. G. Villanueva, and M. L. Roukes, *Fundamentals of Nanomechanical Resonators* (Springer International Publishing, 2016).
[41] M. Sansa, E. Sage, E. C. Bullard, M. Gély, T. Alava, E. Colinet, A. K. Naik, L. G. Villanueva, L. Duraffourg, M. L. Roukes, G. Jourdan, and S. Hentz, Nat. Nanotechnol. **11**, 552 (2016).
[42] A. Hoffman and J. A. Hubbell, *Biomaterials Science: An Introduction to Materials in Medicine* (Academic Press; Elsevier, 2004), p. 225.

Review of Scientific Instruments ARTICLE scitation.org/journal/rsi

Multimodal real-time frequency tracking of cantilever arrays in liquid environment for biodetection: comprehensive setup and performance analysis

Annalisa De Pastina[a)], Francesco Padovani[b)], Giulio Brunetti[a)], Chiara Rotella[a)], Fabio Niosi[a)], Victor Usov[c)], and Martin Hegner[a),*]

[a)] Center for Research on Adaptive Nanostructures and Nanodevices (CRANN), School of Physics, Trinity College Dublin (TCD), D02 Dublin, Ireland
[b)] Institute of Functional Epigenetics, Helmholtz Zentrum München (HMGU), Neuherberg 85764, Germany
[c)] School of Physics, Trinity College Dublin (TCD), D02 Dublin, Ireland
* corresponding author: HEGNERM@tcd.ie

Supplementary Information

Rev. Sci. Instrum. **92**, 065001 (2021); doi: 10.1063/5.0047631

I. CAPILLARY FUNCTIONALIZATION PLATFORM

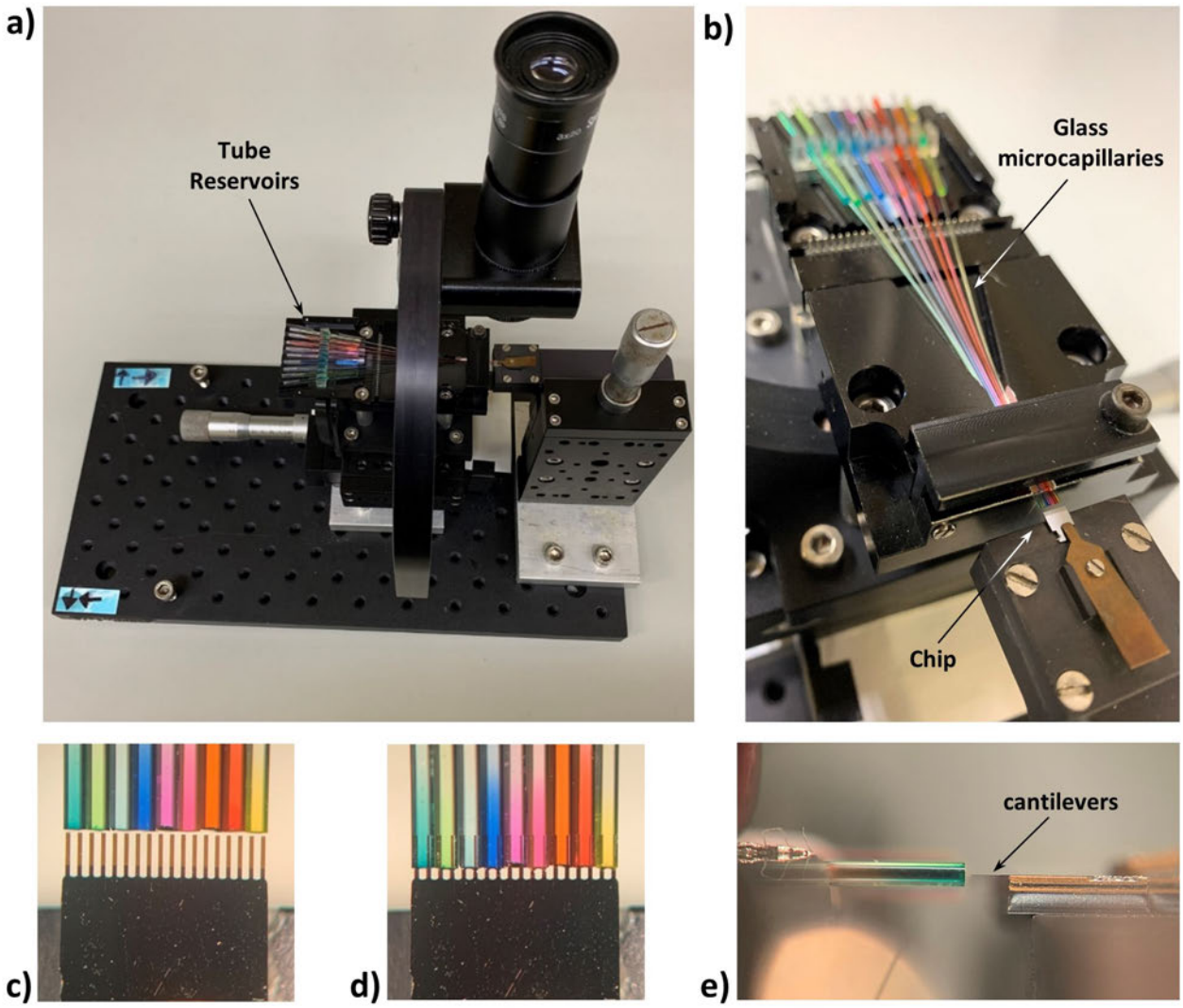

Figure S1: **a)** Home built functionalization platform. **b)** Both microglass capillaries and microcantilever array chip are mechanically clamped and brought in proximity. The end of microcapillaries is inserted into larger glass tubes which serve as fluid reservoirs and facilitate the injection of fuctionalization solutions via manual pipettor. An optical lens (10x magnification) is mounted on a semicircular mechanical guide. This allows to slide the monocular on the guide so to control via top view (**c, d**) and side view (**e**) the alignment between cantilever array chip and the glass microcapillaries. The alignment is achieved via manual xyz micrometer positioning stages.

II. INKJET SPOTTER FUNCTIONALIZATION

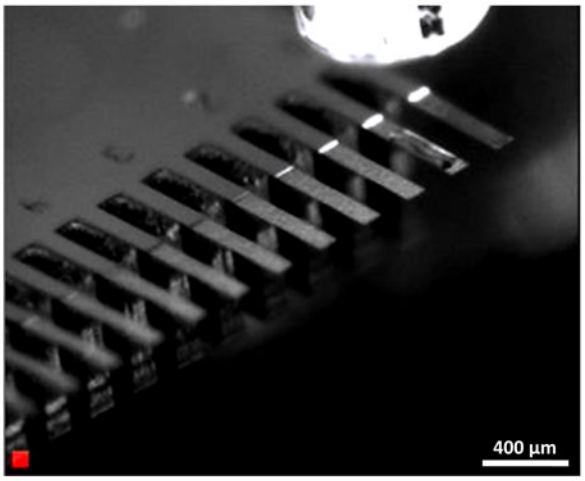

Movie1: Video capture of the functionalization of alternate microcantilevers on a 18-sensors chip. The image above shows ongoing spotting on the second cantilever from the right. 18 sensors can be one side-coated in about 20 seconds with a single autopipet fluid loading (max. 25 µl). Automated dispensing patterns can be programmed by assigning offsets or defining matrix geometries. The video is captured via the inkjet spotting equipment built-in camera.

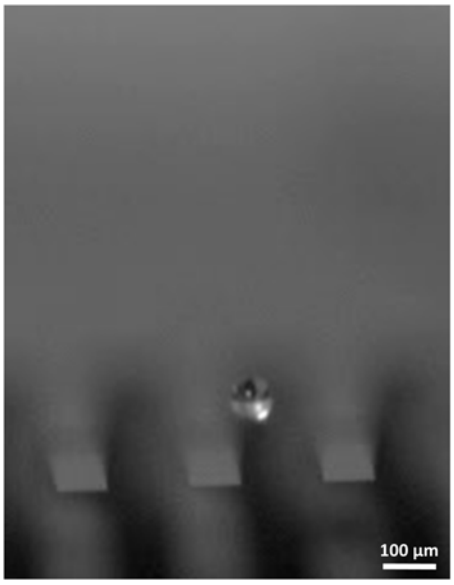

Movie2: High-speed video capture (Phantom v1210 digital high-speed camera, *Vision Research*) of a water droplet inkjet spotted on a silicon microcantilever. By misaligning the droplet with respect to cantilever width center axis, it is possible to achieve double side coating.

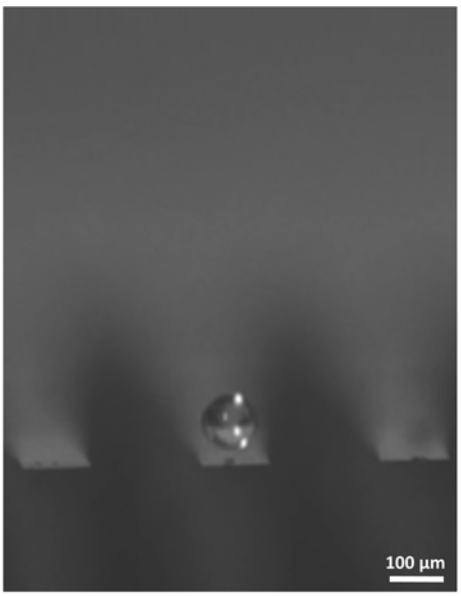

Movie3: High-speed video capture (Phantom v1210 digital high-speed camera, *Vision Research*) of a single water droplet inkjet spotted on a silicon microcantilever and landing on the sensor top surface.

III. SELF ASSEMBLED MONOLAYERS

In order to functionalize the gold surface of the cantilevers with self-assembled monolayers (SAM), the gold-coated chip is removed from the storage box (Argon, 0.07 MPa) and immersed in ethanol (C_2H_6O, HPLC Grade) for 30 minutes. Subsequently, possible organic residues are cleaned via 10 minutes of UV exposure (*Boekel* UV-Ozone cleaner, 135500), which also serves to activate the gold surface and clean it from environmental organics prior to functionalization [1, 2]. The chip is immersed and kept in fresh ethanol until the mounting in the capillary functionalization platforms.

Microglass capillaries and tube reservoirs are cleaned and kept in ethanol solution. Before functionalization, they are dried on filter paper and placed under heat lamp (*Osram SICCATHERM* infrared heat lamp 375 W) for 10', to ensure total removal of ethanol.

Functionalization solutions are prepared as follows (all chemicals are purchased from *Sigma Aldrich, Ireland*):

1) $-CH_3$ terminated SAM: 2mM Hexadecanethiol (MW= 258.51 g/mol) in ethanol solution
2) –PEG terminated SAM: 2mM 11-Mercaptoundecyltetraethylene glycol (MW= 380.58 g/mol) in ethanol solution
3) $-NH_2$ terminated SAM: 2mM 11-Amino-1-undecanethiol (MW= 239.85 g/mol) in ethanol solution
4) –COOH terminated SAM: 2mM 11-Mercaptoundecanoic acid (MW= 218.36 g/mol) in ethanol solution

The chip is incubated in the glass microcapillaries filled with SAM solutions for 10 minutes, and stored in fresh ethanol at 4°C overnight, one day before experiment.

In case of planned bacterial detection, after functionalization the chip would be rinsed in ethanol, nanopure water, and incubated in the same buffer used in the experiment (e.g. HEPES buffer) at 26°C overnight, as explained in the main text.

IV. PIEZOSTACK ACTUATORS

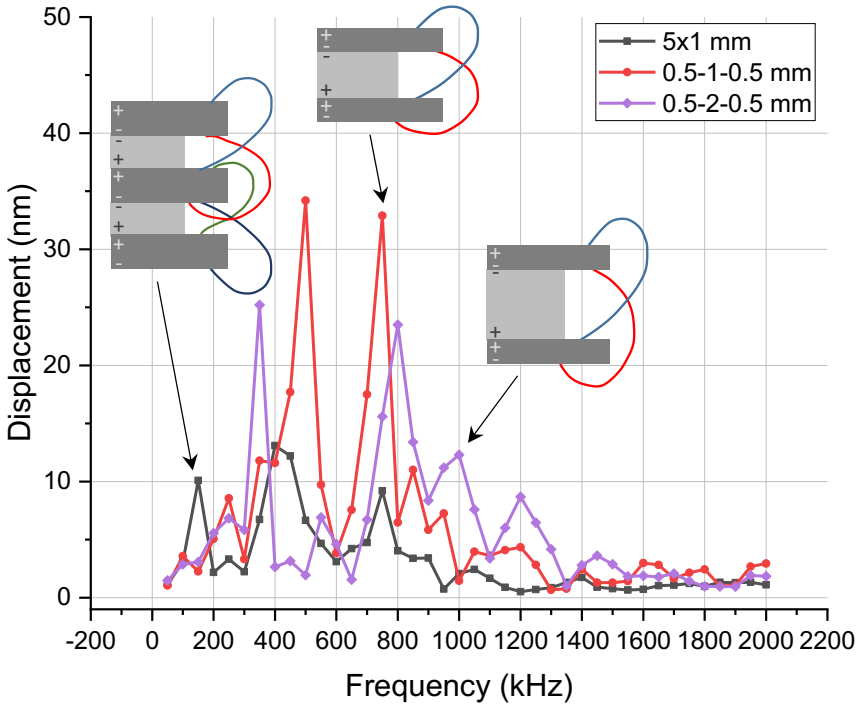

Figure S2: Displacement in air of the 200 µm-thick PEEK membrane, designed to host the cantilever array chip on one side, and the piezostack actuator on the other side. The piezostack is actuated with 1Vpp voltage signal generated via a function generator (DS345, *Stanford Research*) over a frequency range between 50 kHz to 2 MHz. The membrane deflection is detected via a fiber-optic vibrometer (OFV-552, *Polytech*), by focusing the laser spot at the center of the PEEK membrane. Three piezostack actuators configurations are compared, with different number of layers and thickness: a stack of 5 piezoceramic layers, each 1 mm thick (black line); two stacks of 3 piezoceramic layers, with thickness of 0.5/1/0.5 mm (red line) and 0.5/2/0.5 mm, respectively (purple line). For the three devices, the best actuation efficiency is measured between 350 kHz and 1 MHz. A higher number of layers is expected to result into a larger displacement, however the 0.5/1/0.5 mm 3-stack actuator exhibits the largest actuation efficiency. We attribute this outcome to the manual fabrication process, which includes several stages of gluing and alignment, thus affecting the consistency of the final device. However, all devices were integrated into microfluidic measurement chambers, and provided successful actuation of microcantilevers up to 2 MHz, given an actuation voltage between 1 and 5 V.

MECHANICAL SIGNALS

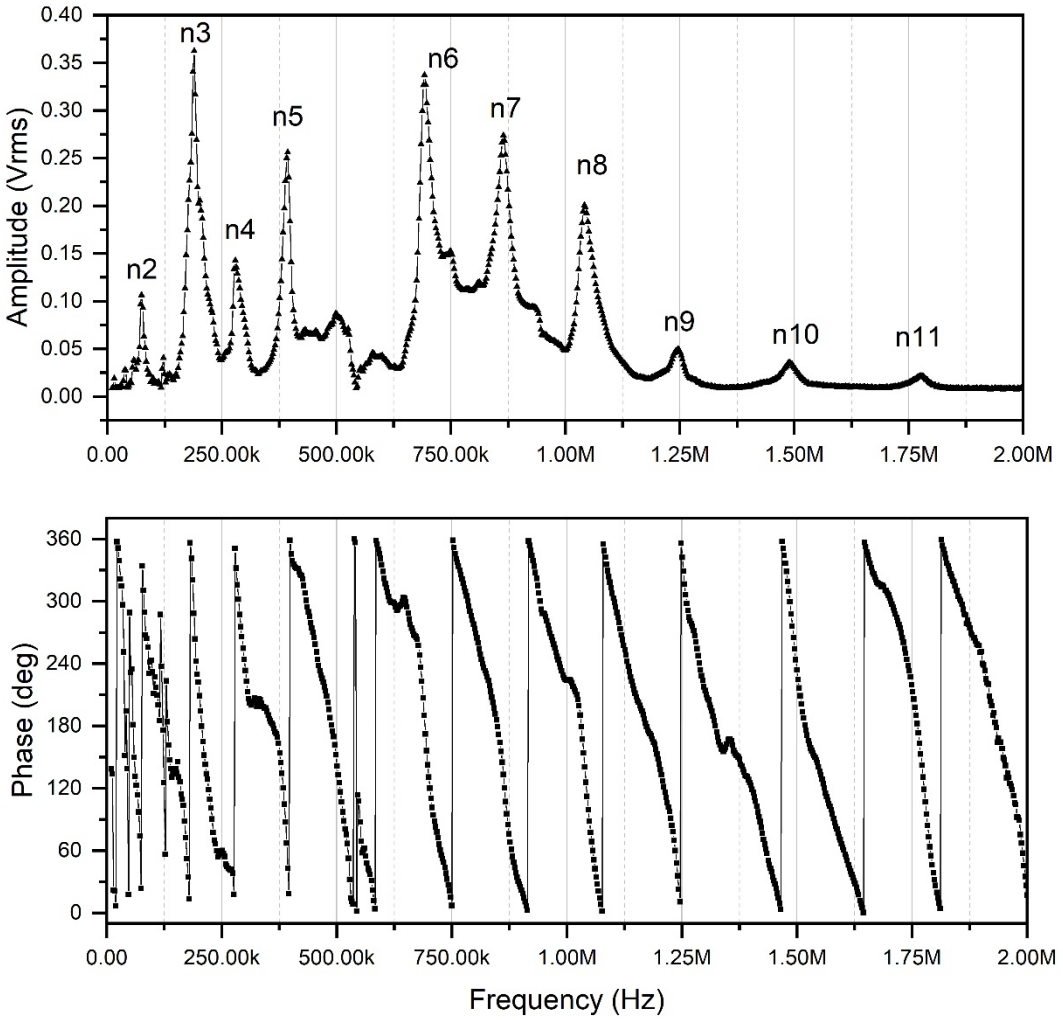

Figure S3: Amplitudes (top) and phase values (bottom) of the first 11 flexural modes of vibration (devices 400 µm long, 2.3 µm thick and 70 µm wide), excited with in-house built piezostack actuators and detected via PSD sensor. The measurement bandwidth extends from 10 Hz to 2 MHz and is currently limited by the piezo actuation stage, as the operational frequency of the piezostack actuator reaches a maximum of 2 MHz, as shown in Figure S2. The resonance frequency values are slightly different when considering 15-cantilevers arrays (see next section), where geometrical dimensions are 500 µm long, 2.3 µm thick and 95 µm wide.

V. OPTICAL READOUT

ELECTRICAL CIRCUIT SCHEMATIC

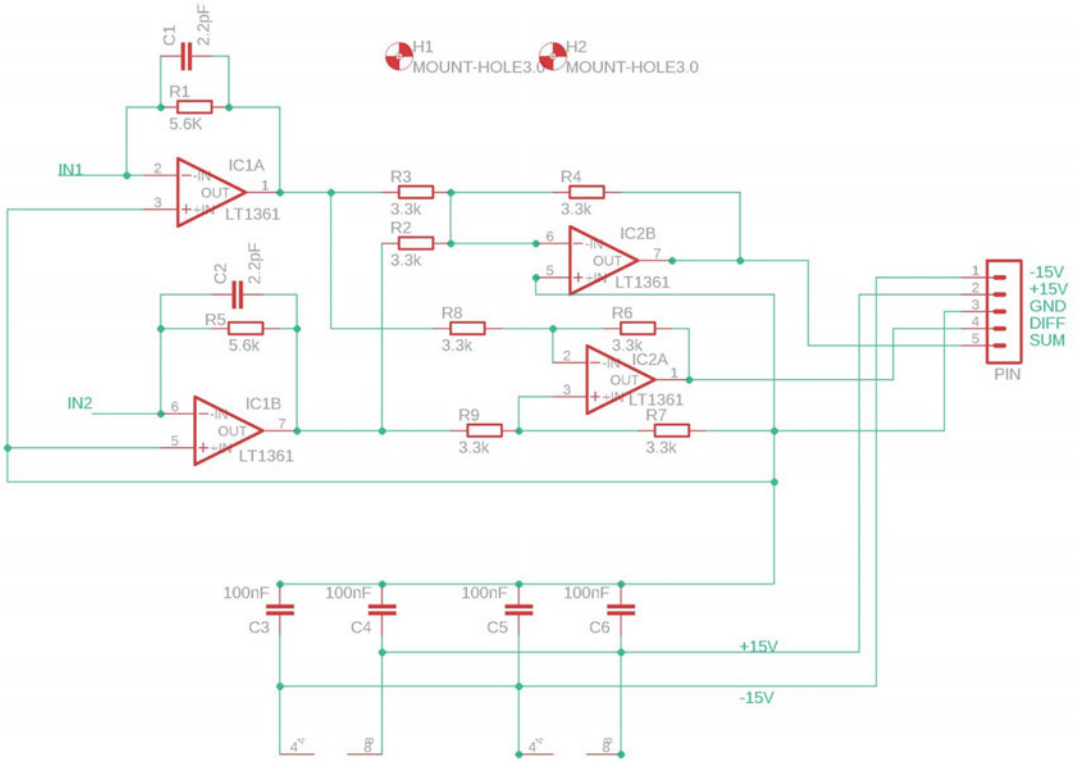

Figure S4: Schematic of the developed electronic circuit for PSD readout. The circuit includes two amplification stages, based on the operational amplifiers LT1361 (*Analog Devices Inc.*): the first stage converts the currents generated by the two PSD electrodes into voltages. Voltages are combined into sum and difference values, through a second amplification stage with gain 1.

The PSD and electronic I-V converter circuit have a final combined cut-off frequency of 4.8 MHz, calculated as in [3], as shown below:

$$BW_{-3dB} = \sqrt{\frac{GBP_{LT1361}}{2\pi\, R_{IV}\, C_{tot}}} = \sqrt{\frac{50\text{MHz}}{2\pi\ 5.6\ \text{k}\Omega\ 60\text{pF}}} = 4.8\ \text{MHz}$$

where:

- GBP_{LT1361} is the gain per bandwidth product, provided in the datasheet of the LT1361 operational amplifier
- R_{IV} is the feedback resistor in the IV conversion stage of the electronic circuit
- C_{tot} is the sum of the PSD capacitance (50 pF), the operational amplifier input capacitance (3pF), parasitic and wire capacitance of the circuit (estimated about 7 pF)

VI. SWEEP VS PLL METHOD COMPARISON

a) b)

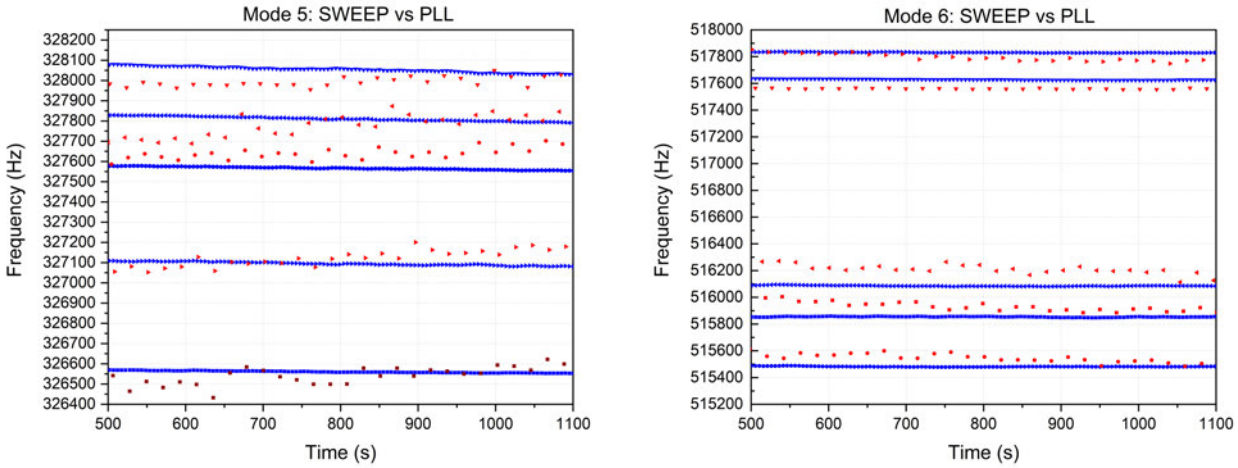

Figure S5: Performance comparison between the former SWEEP method (red data points) and the newly implemented PLL (blue data points). The resonance frequencies (mode 5 **(a)** and mode 6 **(b)**) of a cantilever array (500 µm long, 2.3 µm thick and 95 µm wide) in PBS buffer were acquired for 30 minutes with each method, sequentially. As also shown in Table S1, the PLL is more than 3 times faster than the SWEEP, when considering identical number of sensors and modes. This is due to the fact that the PLL excites a single frequency value per cycle, while the SWEEP provides actuation over a frequency range that has to be wide enough to enable signal fit to a damped resonator model, in order to later extract the resonance frequency value [4].
In addition, when considering the resonance frequency standard deviation over a time window of 10 min (in the order of the time range of interest for our measurements), we observe an improvement in frequency stability of up to 7-fold with the PLL. We expect an improvement of the same magnitude in terms of mass resolution, thus pushing down to about 2 pg the previous SWEEP detection limit of 10 pg [5].

Table S1

		Mode 5	**Mode 6**
10 min stdev [Hz]	SWEEP	39.0 ± 5.3	29.8 ± 4.3
	PLL	6.2 ± 1.5	4.4 ± 2.4
Time resolution* [s]	SWEEP	20	
	PLL	6	

**Considering 10 sensors and 4 resonant modes*

VII. FREQUENCY NOISE: MODE NUMBER AND SURFACE CHEMISTRY EFFECT

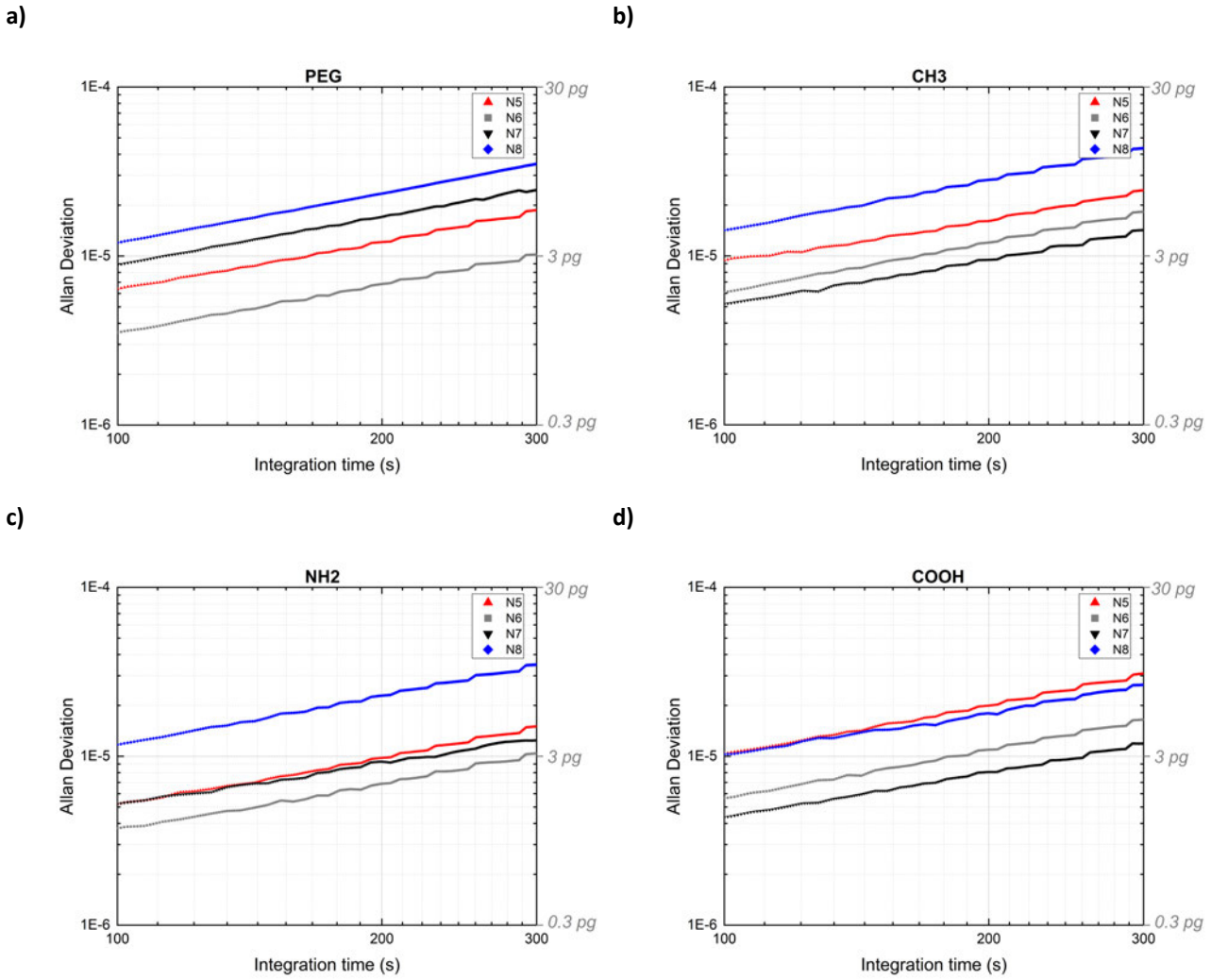

Figure S6: Allan Deviation plots in the time range of interest for devices (400 µm long, 2.3 µm thick and 70 µm wide) in PBS at 26 °C. Each line is the average of 3 sensors functionalized as in section V and with the same molecules, namely hydrophilic (aliphatic thiol molecules terminated with PEG, NH_2 and COOH groups) or hydrophobic (aliphatic thiol molecules terminated with CH_3 group) self-assembled monolayers. All plots show the same linear thermal drift behavior, with Allan deviation slope independent of mode number and functionalization. PEG **(a)**, CH_3 **(b)**, NH_2 **(c)** and COOH **(d)** functionalization do not drastically affect the frequency stability, which lies in the same range, with less than a factor 3 variation, when considering same mode and different interface chemistry.
Considering different mode numbers [N5 (≈450 kHz), red triangles; N6 (≈680 kHz), grey squares; N7 (≈920 kHz), black pointing down triangles; N8 (≈1200 kHz), blue diamonds], it is visible how mode 8 is generally noisier by up to a factor 4, when compared to the better performing modes 6 and 7. At 5 minutes integration time, considering Eq. 3 in the main text, we can estimate a mass resolution between a minimum of 3 pg (mode 6, a) and c)) and and a maximum of 12 pg (mode 8, b)).

VIII. FREQUENCY NOISE INCREASE IN BACTERIAL SOLUTIONS

a)

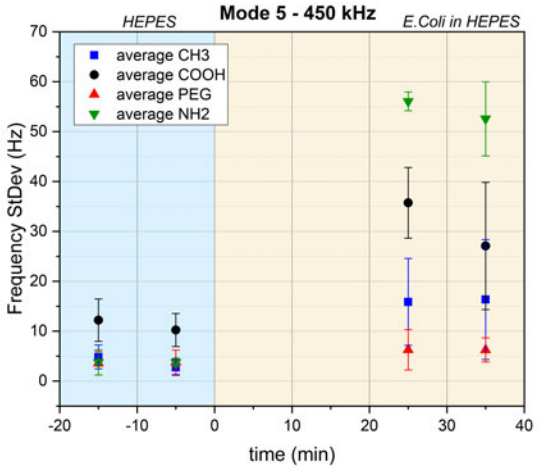

b)

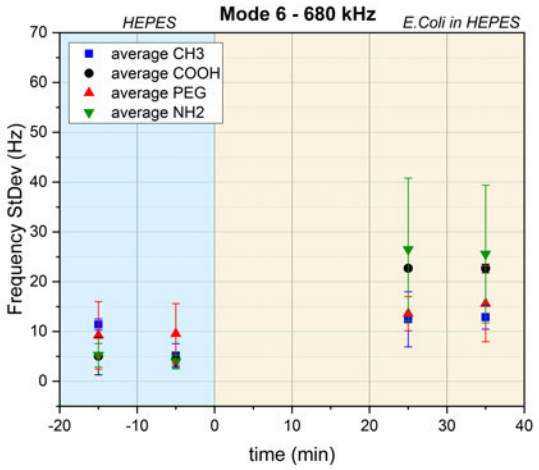

c)

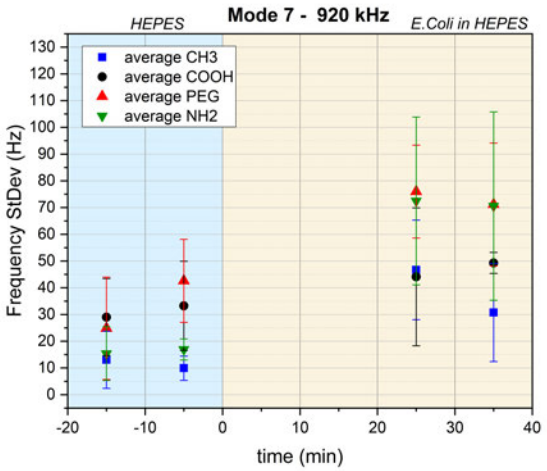

Figure S7: Plot of resonance frequency standard deviation calculated over a time interval of 10 minutes, for cantilever devices (400 µm long, 2.3 µm thick and 70 µm wide) at 26°C. Each data point and relative error bars represent the average value and the standard deviation of 3 cantilevers with same functionalization. Two measurements are collected in HEPES buffer solution (light blue background) and two additional data poits are evaluated after the injection of *E. Coli* bacteria cells in HEPES (light orange background), at a concentration of 10^6cells/µl. For all the modes considered,

N5 **(a)**, N6 **(b)** and N7 **(c)**, the standard deviation shows an increase of up to a factor 4 with respect to the level in buffer. In order to avoid fluidic effects, the measurements in bacteria environment are collected 20 minutes after cells injection in the microfluidic chamber. We attribute this phenomenon to the laser scattering resulting from the presence of bacterial cells moving and floating in the measurement chamber, and in the fluidic space between laser and resonators.

IX. DIFFERENTIAL MASS UPTAKE DERIVATION

As stated in [6] by Sader and Eysden, the n[th] resonance frequency in vacuum $f_{vac,n}$ and fluid $f_{r,n}$ for a cantilever beam immersed in viscous fluid can be written as:

$$\frac{f_{r,n}}{f_{vac,n}} = \left[1 + \frac{\pi\rho b}{4\rho_c h}\Gamma_r^f(Re_n, \kappa_n)\right]^{-1/2} \quad \textbf{Eq. S1}$$

where ρ and ρ_c are the fluid and cantilever mass densities, respectively, b is the cantilever width, h is the cantilever thickness, $\Gamma_r^f(Re_n, \kappa_n)$ is the real component of the hydrodynamic function and depends on the normalized mode number κ_n and on fluid properties through the Reynolds number Re.

$f_{vac,n}$ is expressed as $f_{vac,n} = \frac{1}{2\pi}\frac{\alpha_n^2}{L^2}\sqrt{\frac{EI}{\rho_c bh}}$, where L is the cantilever length, α_n is the n[th] positive root of $1 + cos\alpha_n cosh\alpha_n = 0$, from the Euler Bernoulli beam theory, E and I are the cantilever Young's modulus and second moment of inertia, respectively.

Equation 1 can be rewritten as:

$$\frac{f_{r,n}}{f_{vac,n}} = \sqrt{\frac{4\rho_c h}{4\rho_c h + \pi\rho b\Gamma_r^f(Re_n, \kappa_n)}}$$

and substituting $f_{vac,n}$ with its expression:

$$f_{r,n} = \frac{\alpha_n^2}{2\pi}\sqrt{\frac{EI}{L^4 b\cancel{\rho_c h}} \times \frac{4\cancel{\rho_c h}}{4\rho_c h + \pi\rho b\Gamma_r^f(Re_n, \kappa_n)}} = \frac{\alpha_n^2}{2\pi}\sqrt{\frac{EI}{L^3}\frac{1}{(\rho_c hbL + \frac{\pi\rho b^2 L}{4}\Gamma_r^f(Re_n, \kappa_n)}}$$

where:

- $EI/L^3 = k/3$, and k is the cantilever stiffness
- $\rho_c hbL = m_c$, cantilever mass
- $\pi\rho b^2 L/4 = m_f$, fluid mass loading, calculated as the mass of a fluid cylinder with radius equal to half the cantilever width b

Equation 1 can thus be rewritten as:

$$f_{r,n} = \frac{\alpha_n^2}{2\pi\sqrt{3}}\sqrt{\frac{k}{m_c + m_f\Gamma_r^f(Re_n, \kappa_n)}}$$

Considering a mass uptake Δm due to the binding of target molecules on the sensitized surface of the cantilever, and defining the parameter $\beta_n = \alpha_n^2/(2\pi\sqrt{3})$ we obtain (Equation 1 in main text):

$$f_{1,n} = \beta_n\sqrt{\frac{k}{m_c + \Delta m + m_f\Gamma_r^f(Re_n, \kappa_n)}} \quad \textbf{Eq. S2}$$

where $f_{1,n}$ is the new value of resonance frequency after molecular binding.

The direct expression of Δm can be derived from Equation S2:

$$\Delta m = \frac{k\beta_n^2}{f_{1,n}^2} - m_c - m_f\Gamma_r^f(Re_n, \kappa_n) \quad \textbf{Eq. S3}$$

It is possible to express the differential mass uptake $\Delta m_1 - \Delta m_2$ between two identical cantilevers in the same array (cantilever 1 and cantilever 2) within the same binding event, as follows:

$$\begin{aligned}\Delta m_1 - \Delta m_2 &= \frac{k\beta_n^2}{f_{1,n}^2} - \cancel{m_c} - \cancel{m_f\Gamma_r^f(Re_n, \kappa_n)} - \frac{k\beta_n^2}{f_{2,n}^2} + \cancel{m_c} + \cancel{m_f\Gamma_r^f(Re_n, \kappa_n)} \\ &= k\beta_n^2\left(\frac{1}{f_{1,n}^2} - \frac{1}{f_{2,n}^2}\right)\end{aligned} \quad \textbf{Eq. S4}$$

Eq. S4 (Equation 2 in the main text) allows to compare the binding efficiency, thus the mass uptake, among different sensors while the accurate knowledge about fluidic properties at each measurement point is no longer required.

SMALL MASS ADDITION APPROXIMATION

Eq. S4 can also be reinterpreted as the differential mass uptake among two temporal points on the same cantilever, so that $f_{1,n}$ and $f_{2,n}$ are the n[th] resonance frequency at t=t1 and t=t2.

Under the assumption of small mass addition:

- $\Delta m_1 \approx \Delta m_2 \;\rightarrow\; \Delta m_1 - \Delta m_2 \approx \delta m_n$
- $f_{1,n} \approx f_{2,n} \;\rightarrow f_{1,n} - f_{2,n} \approx \delta f_n$

Equation S4 can thus be rewritten as:

$$\delta m_n = k\beta_n^2\left(\frac{1}{f_{1,n}^2} - \frac{1}{f_{2,n}^2}\right) = k\beta_n^2\left(\frac{f_{2,n}^2 - f_{1,n}^2}{f_{1,n}^2 \cdot f_{2,n}^2}\right) = k\beta_n^2\left(\frac{(f_{2,n} - f_{1,n})(f_{2,n} + f_{1,n})}{f_{1,n}^2 \cdot f_{2,n}^2}\right) \approx$$

$$\approx k\beta_n^2\left(\frac{-\delta f_n \cdot 2f_n}{f_n^4}\right) = -2\frac{\delta f_n}{f_n}\frac{k\beta_n^2}{f_n^2}$$

Knowing that $f_{r,n} = \beta_n\sqrt{\frac{k}{m_c}} \;\rightarrow\; \frac{k\beta_n^2}{{f_n}^2} = m_c$ we obtain:

$$\delta m_n = -2\frac{\delta f_n}{f_{r,n}} m_c \qquad \textbf{Eq. S5}$$

Equation S5 (Equation 3 in the main text) can be used to estimate the mass resolution δm_n, from the knowledge of the frequency stability $\frac{\delta f_n}{f_{r,n}}$, measured via Allan deviation analysis.

REFERENCES:

[1]H. Ron, S. Matlis and I. Rubinstein, Langmuir **14,** 1116 (1998).
[2]D. L. Allara, Biosensors and Bioelectronics **10,** 771 (1995).
[3]T. Fukuma, Review of Scientific Instruments **80,** 023707 (2009).
[4]S. Schmid, L. G. Villanueva and M. L. Roukes, *Fundamentals of Nanomechanical Resonators* (Springer International Publishing, 2016).
[5]G. Brunetti, F. Padovani, A. De Pastina, C. Rotella, A. Monahan, S. L. Hoffman, S. A. Jongo, S. Abdulla, G. Corradin, G. Pluschke, C. Daubenberger and M. Hegner, Nanoscale **13,** 2338 (2021).
[6]C. A. V. Eysden and J. E. Sader, Journal of Applied Physics **101,** 044908 (2007).